Article

Current Biology

Algorithmic dissection of optic flow memory in larval zebrafish

Graphical abstract

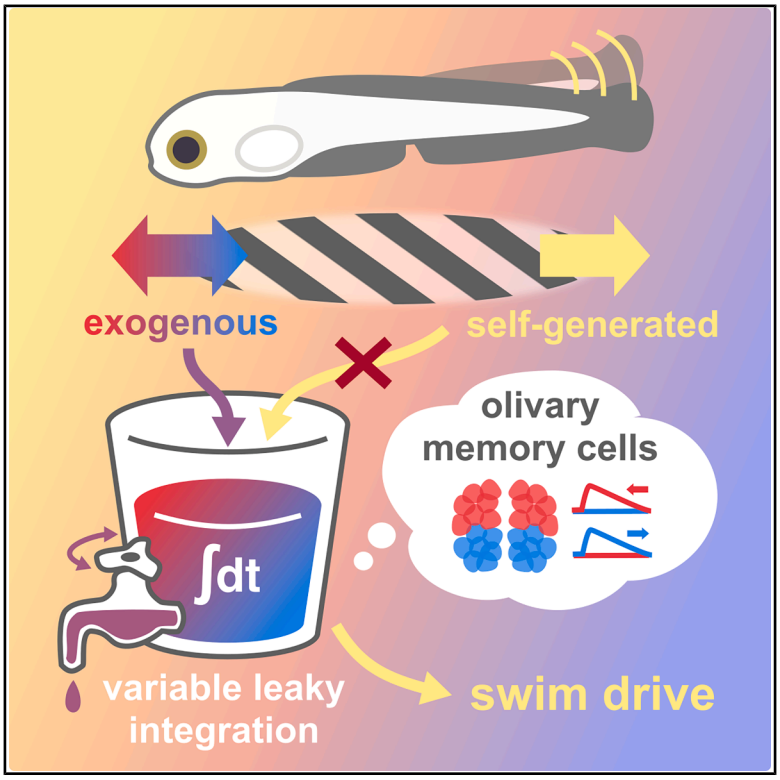

Highlights

- Larval zebrafish use exogenous optic flow seconds ago for stabilization swimming
- The memory-based stabilization involves multiple timescales
- Neurons with signatures of reafference cancellation found across brain regions
- A model connects memory-like olivary activities to behavioral timescales

Authors

Ryosuke Tanaka (田中 涼介),
Ruben Portugues

Correspondence

ryosuke.tanaka@tum.de (R.T.),
ruben.portugues@cornell.edu (R.P.)

In brief

Hysteretic optomotor responses in larval zebrafish have emerged as a simple model of working memory and decision-making. Tanaka and Portugues dissect their algorithm with psychophysics, revealing its reafference selectivity and multiple timescales. Calcium imaging and computational models further constrain the neural mechanisms underlying these algorithms.

Tanaka & Portugues, 2025, Current Biology *35*, 4870–4881
October 20, 2025
https://doi.org/10.1016/j.cub.2025.08.047

CellPress

CellPress
OPEN ACCESS

Current Biology

Article

Algorithmic dissection of optic flow memory in larval zebrafish

Ryosuke Tanaka (田中 涼介)[1,*] and Ruben Portugues[1,2,3,4,5,6,*]
[1]Institute of Neuroscience, Technical University of Munich, Biedersteiner Str. 29, 80802 Munich, Germany
[2]Munich Cluster of Systems Neurology (SyNergy), Feodor-Lynen-Str. 17, 81377 Munich, Germany
[3]Bernstein Center for Computational Neuroscience, Großhaderner Str. 2, 82152 Planegg-Martinsried, Germany
[4]Max Planck Fellow Group, Mechanisms of Cognition, MPI Psychiatry, Kraepelinstr. 2-10, 80804 Munich, Germany
[5]Department of Neurobiology and Behavior, Cornell University, 215 Tower Road, Ithaca, NY 14853, USA
[6]Lead contact
*Correspondence: ryosuke.tanaka@tum.de (R.T.), ruben.portugues@cornell.edu (R.P.)
https://doi.org/10.1016/j.cub.2025.08.047

SUMMARY

The visual stabilization behavior in the larval zebrafish reflects the history of optic flow experienced in the recent past. This integrative process has gained traction in recent years as a simplified, tractable model of working memory and decision-making. Yet its algorithmic bases are poorly understood. In this study, we first demonstrate that only externally generated, but not self-generated, optic flow contributes to future history-dependent stabilization behaviors. This observation suggests that the hysteresis in the stabilization behavior reflects a sensory low-pass filtering process rather than the self-location memory achieved through path integration. Second, through reverse correlation and delay-based paradigms, we reveal multiple timescales involved in the integration of optic flow. With the help of quantitative modeling, we show that the fish becomes more forgetful about the past optic flow in a more dynamic visual environment. Next, with whole-brain, light-sheet calcium imaging, we find optic-flow-selective neurons that exhibit signatures of motor efference copies in various brain regions, mirroring the behavioral findings. Lastly, with two-photon calcium imaging, we show that inferior olive neurons integrate forward and backward flow separately, giving clues about how the multiple timescales of optic flow integration are implemented. Overall, the results here refine our algorithmic and functional understanding of the history dependence of the visual stabilization behaviors in the larval zebrafish, paving the way for deciphering its circuit implementations.

INTRODUCTION

The behaviors of animals reflect not only the incoming sensory inputs but also the history of sensory events. How a brain, which is composed of neurons operating at the timescale of milliseconds, can retain information over a longer timescale of seconds is not trivial and has attracted researchers' attention.[1–3] A relatively simple example of such history-dependent behaviors is the optomotor response (OMR) in the larval zebrafish—one of the smallest vertebrate model organisms in modern neuroscience. When presented with patterns of wide-field visual motion indicative of observer movements (i.e., optic flow[4]), various animal species, including the larval zebrafish, exhibit body movements to stabilize their heading and position, a behavior called OMR.[5–8] Recently, it has been shown that the OMR of the larval zebrafish can be affected by optic flow that happened many seconds ago.[9–14] These studies also made converging observations regarding the potential neural loci for integration of optic flow, including the interpeduncular nucleus, medulla oblongata, and inferior olive (IO).

By contrast, it remains unclear what this integrative process estimates. Some argued that the fish integrate optic flow to improve their estimate of the direction and speed of the environmental flow in the face of sensory noise.[9,11] Others suggested that the fish estimates self-location through visual path integration, akin to what is achieved in the mammalian hippocampal formation.[14] The former flow estimation account would predict that self-generated optic flow does not count toward the optic flow memory because self-generated optic flow is not directly informative about the flow in the environment. On the other hand, the latter, self-location memory account predicts that both exogenous and self-generated flow should contribute to the optic flow memory. So far, these two possibilities have not been experimentally tested.

The primary goal of this study is to dissect the algorithms involved in the second-scale integration of optic flow to better understand their functions. First, by manipulating the gains of visual feedback, we demonstrate that the history-dependent component of the OMR depends only on the externally generated (i.e., exafferent) optic flow, but not on the self-generated (i.e., reafferent) optic flow. This pattern holds for both position- and heading-stabilizing OMR and is more consistent with the flow estimation account. Second, we characterize the dynamics of the history dependence in the OMR using reverse correlation and delay-based paradigms. Unexpectedly, the two approaches uncovered different timescales, suggesting that

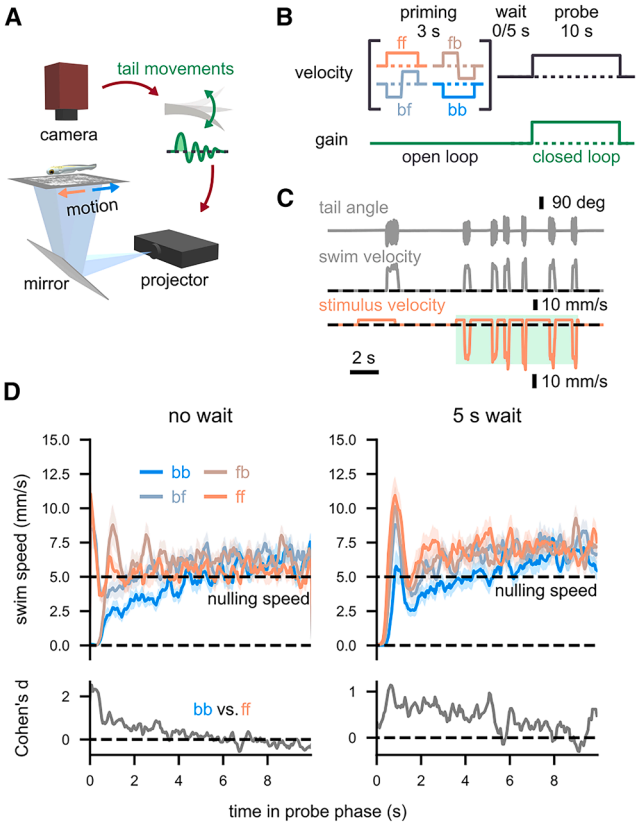

Figure 1. Forward OMR depends on the history of optic flow

(A) A schematic of the behavioral setup.

(B) A schematic of the priming-delay assay. The priming phase came in four conditions: forward-forward (ff), forward-backward (fb), backward-forward (bf), and backward-backward.

(C) An example trial from a single fish. The dotted horizontal lines indicate 0. The green-shaded region represents the closed-loop probe phase.

(D) Top: average swim speed in the probe phase color-coded by priming conditions. Dotted horizontal lines indicate 0 mm/s and the nulling speed of 5 mm/s (i.e., the speed at which the exafference is exactly canceled). Bottom: Cohen's d between forward- and backward-priming conditions, calculated across the population. Trials with and without the 5-s delay period are plotted separately. The solid lines and the shaded areas respectively indicate the mean across fish and its standard error. $N = 30$ fish.

See also Figure S1 and Table S1.

the fish becomes more forgetful in a more dynamic environment. With whole-brain calcium imaging with light-sheet microscopy, we find optic-flow-selective neurons that receive motor efference copy signals counteracting the reafferent visual inputs across various brain regions. Finally, with two-photon calcium imaging, we show that neurons in the IO integrate forward and backward optic flow separately with long time constants, providing clues to how the multiple timescales of the history-dependent OMR are implemented.

RESULTS

Forward OMR is dependent on sensory history

To probe the OMR and its history dependence in the zebrafish larvae, we utilized a head-restrained, closed-loop behavioral assay as described before[15] (see STAR Methods for details). Briefly, 6- to 8-day-old larvae were head fixed in low-melting-point agarose with their tail free to move and observed visual stimuli projected below with a small projector (Figure 1A). The movements of the tail were monitored with a high-speed camera, which was then used to infer intended swim patterns and to provide real-time visual feedback. In the first set of experiments, we focused on forward swimming in response to forward optic flow. Visual patterns flowing forward give the impression that the observer is drifting backward relative to the environment and elicit a robust OMR in larval zebrafish.[15] Throughout the paper, we will describe optic flow in terms of the directions of movements of the visual patterns as seen from the fish's perspective, as opposed to the directions of the implied observer movements.

In the initial experiment, we performed an optic flow memory assay similar to the ones used in Yang et al.[14] (Figure 1B). In each trial, fish first observed 3 s of visual flow moving either forward or backward at 5 mm/s, with a possible directional switch in the middle ("priming" phase). This priming phase was in an open loop: that is, tail movements did not affect the ongoing visual stimuli. After an open-loop delay period without visual motion for either 0 or 5 s, the fish then entered the probe phase, where forward flow at 5 mm/s was presented for 10 s. During the probe phase, the tail beats of the larvae were translated to backward movements in the visual patterns (i.e., closed loop) (Figure 1C) (see STAR Methods for the details). We observed effects of the priming directions on the swimming speed during the probe phase (Figures 1D and S1A), revealing the history dependence of the forward OMR. In particular, the instantaneous swim velocity was higher in the forward-priming conditions compared with the backward condition up until several seconds into the probe phase (with medium effect sizes of Cohen's d = 0.5), for both 0- and 5-s waiting conditions (Figure 1D). The direction-switching priming conditions resulted in intermediate behaviors. These results essentially replicate the observations by Yang et al.,[14] but in non-paralyzed fish.

Self-generated optic flow does not count toward the future OMR

Optic flow can arise as a consequence of active movements of the observer (i.e., reafference) or from passive movements of the observer due to environmental perturbations (i.e., exafference), such as water flow or wind. If the purpose of the integration of optic flow is to low-pass filter the sensory input and better estimate the velocity of the environmental flow ("flow estimation" account),[9,11] then only exafferent, but not reafferent, optic flow should be integrated. Alternatively, if fish are trying to go back to the original position by integrating optic flow ("self-location memory" account),[14] then they should integrate both reafferent and exafferent optic flow.

To disambiguate these two possibilities, we next explicitly manipulated the reafferent optic flow while keeping the exafference constant (Figure 2A). Each trial started with 5 s of the priming phase, where 5 mm/s forward optic flow was presented. After a delay of 2 s, 5 mm/s forward optic flow was presented again for 10 s ("probe"). Here, the priming phase was in a closed loop, and the probe phase was in an open loop, unlike in the previous experiment (Figure 1). In addition, the gain of the closed-loop

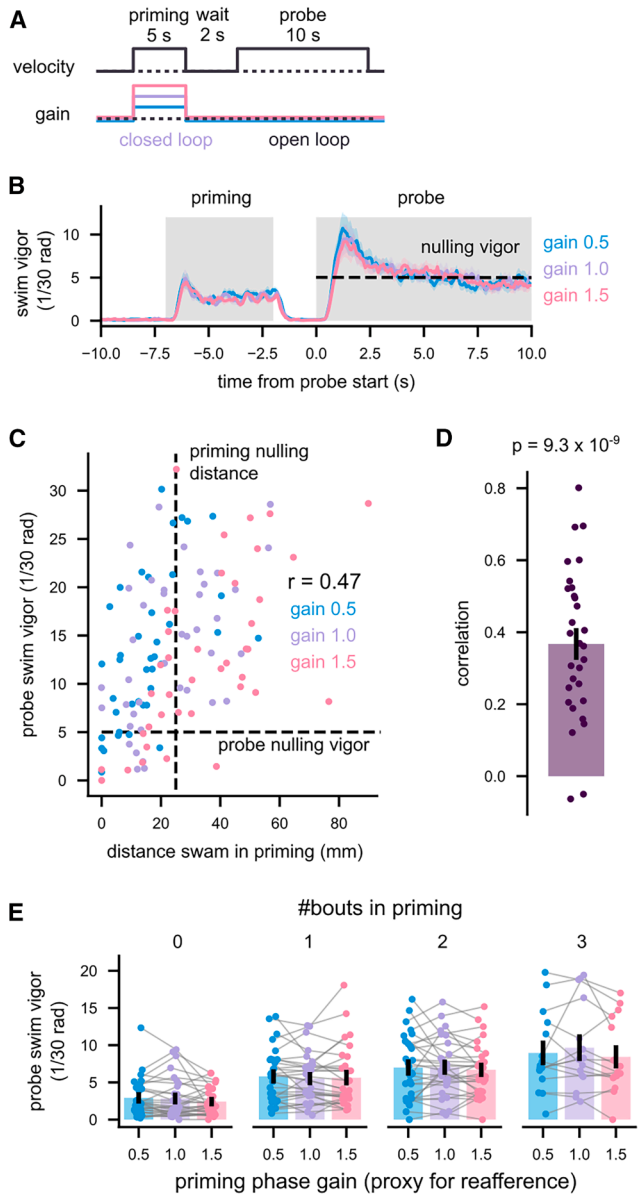

Figure 2. Forward OMR depends on the history of exafferent optic flow

(A) A schematic of the protocol.

(B) The population-average swim vigor (i.e., rolling standard deviation of the tail angle) over time throughout the trial. The vigor is scaled so that the number could also be read as speed in mm/s assuming a gain of 1.0. Shaded areas represent standard errors of the mean. The dotted horizontal line indicates the vigor at which the exafference would be canceled if there was closed-loop feedback of 1.0 gain.

(C) Trial-by-trial data from an example fish. Swim speeds averaged over time during the probe period (assuming 1.0 gain) are plotted against the distance swam during the priming period. Each dot corresponds to a trial. The horizontal dotted line indicates the swim vigor that would cancel the exafference if there was 1.0 gain, and the vertical dotted line indicates the priming distance swim that would cancel the exafferent displacement.

(D) Pearson correlation between the probe speed and priming swim distance from all fish. $N = 30$ fish. The p value is from a signed-rank test against 0.

(E) Trial-averaged probe swimming speed as functions of the priming gain and the number of bouts during the priming. The bars indicate the average across fish, and the dots individual fish. The data from identical fish are connected. For any given number of priming bouts, no significant difference in probe swim speed by the priming phase gain was detected with Friedman's chi-squared tests ($p > 0.05$). $N = 30$, 30, 29, and 15 for # bouts = 0, 1, 2, and 3. N is smaller than 30 in some conditions because some fish did not have trials with the same number of bouts across all three gain conditions.

See also Figure S1 and Table S1.

feedback was either increased to 1.5 or decreased to 0.5 in some trials. Thus, the fish always received a fixed amount of exafferent optic flow in each priming phase but different amounts of reafferent optic flow, depending on their behavior and the closed-loop gain. We made sure that the fish were aware of this gain manipulation by comparing the bout durations (Figure S1B).

Figure 2B shows the swimming effort of the fish over time. While the prolonged exposure to gain manipulations has been shown to affect their future OMR drive,[16] this effect was on average not apparent, likely because our priming phases were short. Figure 2C shows the trial-by-trial data from a representative single fish. In this fish, more swimming in the priming phase led to more swimming in the probe phase. This positive correlation between the priming and probe phase swimming was consistent across the tested population (Figure 2C). Note that neither of the aforementioned functional interpretations predicts the positive priming-probe correlation: the flow estimation account predicts that the reafferent optic flow seen during the priming phase would be ignored for the future OMR (i.e., no correlation). The path integration account predicts that more swimming in the priming phase would lead to less swimming in the probe phase (i.e., negative correlation).

This positive correlation can trivially result from any type of temporal autocorrelation in the likelihood of the fish to behave (i.e., behavioral states). For example, in some trials, fish might be more alert in general and swim more in both phases, and some other times, they might sleep through the trial. To isolate the effect of the reafferent optic flow from the effect of behavioral states, we sorted the trials by the number of swim bouts in the priming phase (Figure 2D). Even among the trials with the same number of priming bouts, we still did not observe the effects of the amount of the reafference (proxied by the priming phase closed-loop gain) on the probe phase swimming. In other words, the history-dependent OMR does not depend on the reafferent optic flow. This observation is more consistent with the flow estimation account than the self-location memory account. We also made sure that the observed lack of the reafference effect is not due to the open-loop probe phase (Figures S1C–S1G).

The rotational OMR also depends only on exafferent optic flow

The experiments so far established that the forward OMR is dependent on the history of exafferent but not reafferent optic flow. We next wondered whether the same holds for other types of OMR. Rotational optic flow in yaw directions triggers whole-body rotation in various teleost fish,[17,18] which we will refer to as the rotational OMR. First, we established that the head-restrained zebrafish larvae show robust rotational OMR, whose magnitude was roughly proportional to the stimulus angular velocity, albeit with a low gain (Figures S2A–S2C). Next, we performed a priming-delay assay similar to Figure 1B in the

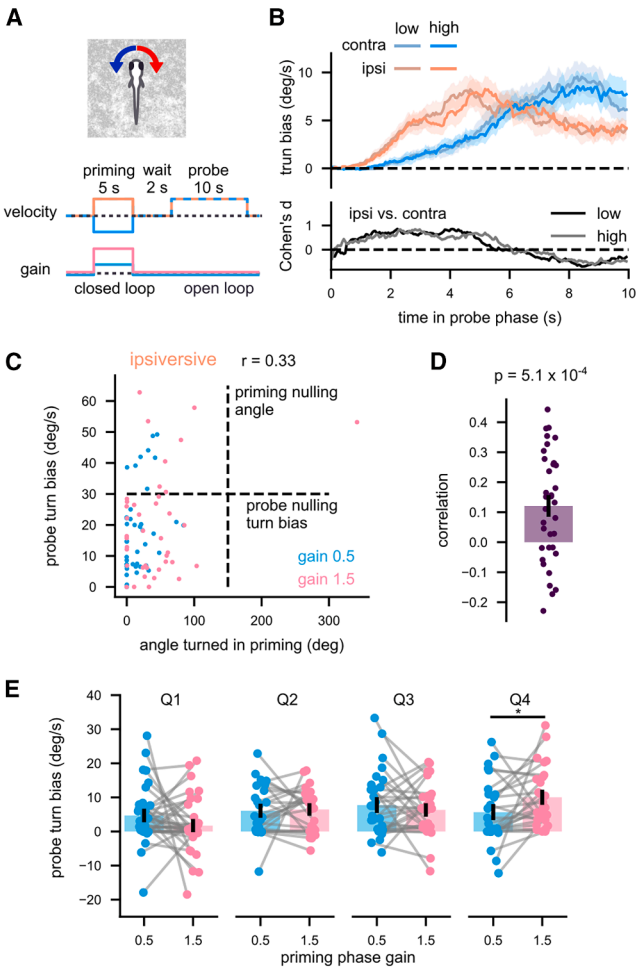

Figure 3. Rotational OMR depends on the history of exafferent optic flow

(A) A schematic of the protocol.

(B) Top: average turning bias during the probe phase. Bottom: Cohen's d between ipsi- and contra-directional conditions within each gain condition over time. The solid lines are the averages across fish, and the shaded areas indicate the standard errors of the means.

(C) Data from an example fish in ipsi-directional priming conditions. Swim bias during the probe period (i.e., smoothed bout bias) is plotted against the angle turned during the priming period. Each dot corresponds to a trial. The vertical dotted line indicates the angle that cancels the exafferent priming rotation. The horizontal dotted line indicates the turn bias that would cancel the visual rotation if there was a gain of 1.0 feedback in the probe phase.

(D) Pearson correlation between the probe speed and priming swim distance from all fish. The bar indicates the average across fish, and the dots are individual fish. The p value is from a signed-rank test against 0. $N = 36$ fish.

(E) Trial-averaged probe turn bias stratified into quartiles based on the angles turned during the priming phase, disregarding the gains. The data from identical fish are connected. Only data from ipsi-directional conditions are plotted. See Figure S3 for the contra-directional data. Pairwise signed-rank tests detected a significant gain effect only in the fourth quartile (Q4), but in the opposite direction as expected from the self-location memory account. $N = 35$, 25, 29, and 27 for Q1, 2, 3, and 4. $^{*}p < 0.05$.

See also Figures S2 and S3 and Table S1.

rotational dimension (Figure S2D). We found that when the priming stimulus rotated in the same direction as the probe stimulus (i.e., ipsi-directional), the fish performed rotational OMR more compared with when the probe moved in the opposite direction (i.e., contra-directional) (Figure S2E). This effect was significant even after waiting for 5 s, establishing the history dependence of the rotational OMR.

We then asked whether the fish integrated only exafferent or total rotational optic flow for the rotational OMR with a gain-manipulation assay similar to Figure 2. This was of particular interest because the brain of larval zebrafish is equipped with head direction neurons,[19] which are in principle suited for implementing visual path integration in the angular dimension. Each trial started with a 5-s-long closed-loop priming phase, where 30°/s rotational optic flow in either direction was presented. Followed by a 2-s waiting period, another 10 s of 30°/s rotation was presented in an open loop (probe) (Figure 3A). The gain of closed-loop feedback in the priming phase was either low (0.5) or high (1.5). Consistent with the prior experiment (Figures S2D and S2E), the ipsi-directional priming resulted in more rotational OMR in the probe phase (Figure 3B), while the effect of feedback gain was qualitatively not apparent. We then analyzed how behaviors during the priming phase affected swimming in the probe phase on a trial-by-trial basis, focusing on the ipsi-directional priming conditions. Figure 3C shows example data from a single fish, similar to Figure 2B. In this fish, more ipsi-directional turning in the priming phase led to more rotational OMR in the probe phase. This positive correlation was statistically significant across the tested population (Figure 3D). This effect is again not predicted by either flow estimation or self-location memory account but can be parsimoniously explained by any form of autocorrelations in the likelihood of the fish to behave. To isolate the effect of the reafference proxied by the gains, we stratified trials by the angles fish turned in the priming phase into quartiles, disregarding gains. In each quartile, fish performed similar amounts of lateralized tail bends but received reafference 3-fold differently depending on gains. Yet in any quartile, increased reafference did not result in reduced probe OMR predicted by the self-location memory account (Figure 3E). The results from the contra-directional priming conditions are more complex due to the fish's tendency to turn consecutively in the same direction,[11] but similarly, we did not detect any effect of the gains (Figure S3). Overall, the rotational OMR, similar to the translational OMR, appears to depend on the history of exafferent optic flow.

Reverse correlation reveals optic flow memory lasting for a couple seconds

The experiments so far established that both forward and rotational OMR depend on the history of exafferent optic flow. Next, we aimed to characterize the kinematics of the history-dependent OMR in an unbiased manner using a reverse correlation technique.[20,21] We presented head-embedded fish with a visual pattern moving either forward or backward at 15 mm/s in an open-loop fashion. The direction of the motion flipped stochastically following a Poisson point process with the rate of 0.5 Hz (Figure 4A). We then calculated the average of the stimulus velocity time traces leading up to forward swimming bouts, weighted by the peak speed of the bouts (see STAR Methods for details). We refer to this weighted average trace of velocity as a bout-triggered average (BTA) stimulus, which can be

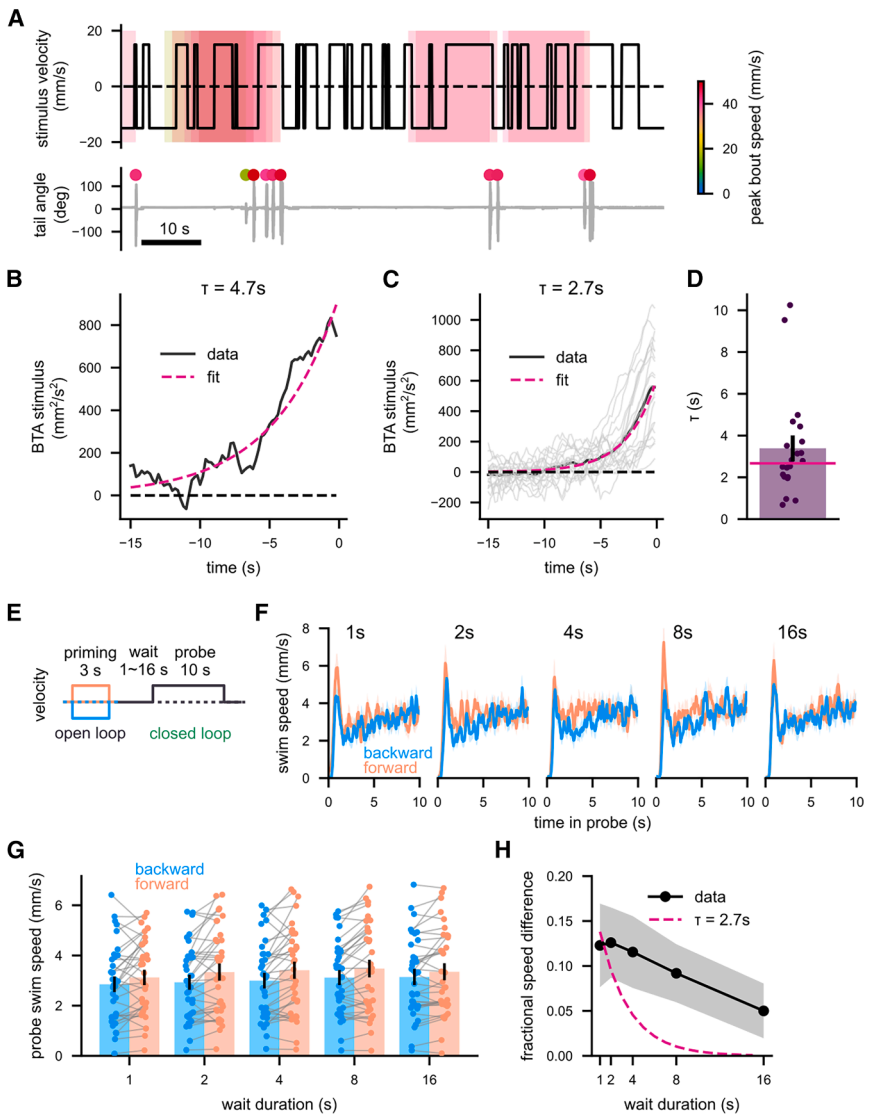

Figure 4. Multiple timescales of history-dependent OMR

(A) Example traces of (top) stimulus velocity and (bottom) tail angles during the reverse correlation experiment. Bouts and velocity traces leading up to them are indicated by dots and boxes colored according to the bout speed.

(B) The BTA velocity trace from the fish in (A) (black) and an exponential fit (magenta).

(C) The BTA stimuli from individual fish (gray) as well as their population average (black). A decaying exponential was fit to the group average (magenta), yielding the time constant (τ) of 2.7 s.

(D) The time constants of the exponential fits to the individual BTA (purple), as well as the time constant of the exponential fit to the population average (magenta line).

(E) A schematic of the long delay experiment.

(F and G) The population-average swim velocity in the probe phase (F) over time and (G) time-averaged, color-coded by the direction of the priming stimuli and sorted by waiting durations.

(H) Fractional differences in the probe swim speed by the conditioning directions, as a function of the wait duration (black), alongside an exponential with the 2.7-s decay constant (magenta).

(C and D) $N = 21$ fish. (F–H) $N = 35$ fish. Each dot in scatterplots indicates a single fish, the bars indicate averages across fish, and the error bars are standard errors of the mean. The solid line and the shaded areas indicate the mean across fish and its standard error.

See also Figure S4 and Table S1.

interpreted as an estimate of the filtering processes happening in the larval brain.

Figures 4B and 4C show BTA stimuli from an individual fish as well as averaged across the population. The population-average BTA was fit well by a decaying exponential with the time constant of 2.7 s (Figure 4D). We performed an equivalent experiment for the rotational OMR and obtained a comparable time constant (Figures S4A–S4D). We made sure with a simulation that this time constant does not simply result from the autocorrelation of the stimulus (Figure S4E). Overall, it appears that both forward and rotational OMR have history-dependent components with the time constant of around 3 s.

The conditional leak model captures the two timescales of optic flow integration

While the time constant of around 3 s is in line with some previous reports,[9,11,12] others have observed much longer history dependence spanning tens of seconds.[14] To make sure that this large discrepancy in timescales did not result from differences in experimental setups, we repeated the priming-delay assay as in Figure 1 with various delay durations between 1 and 16 s (Figures 4E and 4F). We then plotted the difference in the probe swim speed between forward- and backward-priming conditions as a function of the delay durations (Figures 4G and 4H). We found that the probe speed difference by the priming direction only fell from 12% to 6% after 16 s of delay, a kinematics much slower than the reverse correlation-based BTA.

What difference between the two experiments (Figures 4A and 4E) led to these dramatic differences in the observed timescales of the OMR? In the reverse correlation experiment, the fish continuously observed optic flow changing directions, while in the priming-delay assay, the fish did not see any visual motion in the delay phase. Thus, we hypothesized that the presence of concurrent optic flow somehow makes the fish more forgetful about the past optic flow. As a more quantitative expression of this hypothesis, we built a simple dynamical model, which we refer to as the conditional leak model (Figure 5A) (STAR Methods). Similar to the previous models,[9,11] our model unit receives the velocity of optic flow as its input and integrates it in a leaky fashion. The activity of the model unit is subjugated to a static, bounded nonlinearity to generate the rate of stochastically generated swim bouts. In addition, the leakiness is increased if the input speed is above a certain threshold, allowing the system to have different time constants in

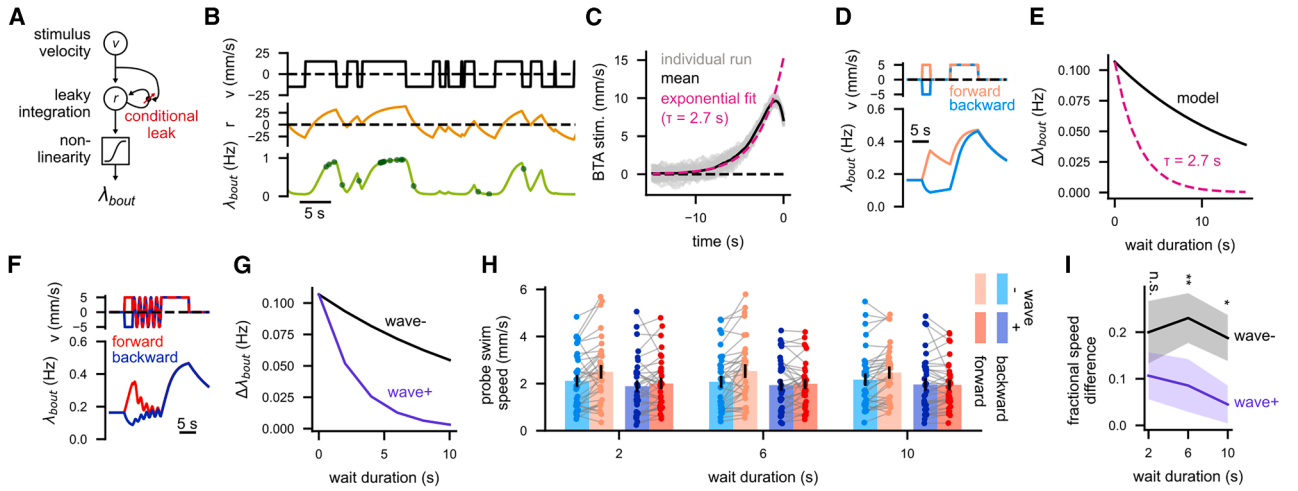

Figure 5. The conditional leak model reconciles the two timescales of OMR

(A) A schematic of the conditional leak model.

(B) An example response of the model to the stochastic direction flip stimulus as in Figure 4A. The yellow line represents the model neuron response, and the green line the bout rate after the nonlinearity. The green dots represent simulated bouts.

(C) Reverse correlation-based BTA stimulus from the model.

(D) Bout rate λ_{bout} calculated by the model in response to the priming protocol.

(E) The difference in mean λ_{bout} during the probe phase by the priming direction as a function of waiting time, as in Figure 4H.

(F and G) Same as (D) and (E), but with the "wave" with net-zero displacement added to the waiting phase. The wave opens the "gate" in the model and reduces the effective time constant of the integrator.

(H) Time-averaged swim speed of real fish during the probe phase as a function of waiting duration, sorted by priming durations and wave conditions.

(I) Fractional differences of the probe swim speed by the priming directions, as functions of waiting durations, sorted by the wave conditions. Each dot in scatterplots indicates a single fish, the bars indicate averages across fish, and the error bars are standard errors of the mean. The solid line and the shaded areas indicate the mean across fish and its standard error. $N = 34$ fish, n.s., not significant ($p > 0.05$), $^{*}p < 0.05$, $^{**}p < 0.01$. p values are from signed-rank tests.

See also Figure S5 and Table S1.

the presence and absence of optic flow. While this model is primarily meant to be phenomenological, implementing such stimulus-dependent modulation of leakiness would also be biophysically feasible, for example, with ligand-gated chloride channels (e.g., γ-aminobutyric acid $[GABA]_A$).[22] By appropriately choosing the model parameters, the conditional leak model can replicate a reverse correlation-based BTA with a relatively short timescale (Figures 5B and 5C) as well as a longer history dependence in a simulated priming-delay assay (Figures 5D and 5E), as expected by construction.

A non-trivial, testable prediction from the conditional leak model is that even a sequence of optic flow that implies net-zero displacement can affect the future OMR by making the fish more forgetful. For example, if we inject a sinusoidally oscillating pattern of velocity inputs with the zero mean to the conditional leak model during the wait phase of the priming-delay assay (Figure 5F), the probe bout rate difference by priming directions decays much faster, following the shorter time constant (Figure 5G). In the real fish, we also observed that oscillating the visual pattern back and forth during the wait phase makes the fish more forgetful (Figures 5H and 5I). For example, the forward OMR of fish was barely affected by the priming directions when the delay phase was longer than 6 s. In a separate experiment, we tested how various types of dynamic visual patterns affect the decay of the optic flow memory (Figure S5). In summary, we found that the optic flow integration in the larval zebrafish involves multiple timescales controlled by the existence and absence of concurrent optic flow.

Direction-selective cells across the brain receive efference copy signals

One of the key insights from the behavioral experiments above is that the hysteretic component of the OMR depends on the exafferent optic flow (Figures 2 and 3). This implies that the responses of optic flow-tuned neurons to expected reafference are canceled by motor efference copy signals somewhere along the pathway that generates the OMR. To identify such efference copy signals in the brain, we performed a brain-wide calcium imaging experiment. Here, we imaged the brains of the larvae broadly expressing a calcium indicator in a nuclear-localized fashion (elavl3:H2B-GCaMP6s) with a light-sheet microscope (Figure 6A). At the beginning of each experiment, we presented the fish with visual patterns moving in the four directions (forward, backward, left, and right) repeatedly and selected neurons that reliably responded to them in a direction-selective fashion (Figures S6A and S6B; see also STAR Methods for the detailed selection criteria). This revealed stereotyped clusters of direction-selective neurons in areas including the pretectum, anterior hindbrain, and IO, as has been previously observed (Figure 6B).[23–25] During the rest of the experiment, the fish experienced a slow (5 mm/s), continuous forward optic flow. Every time the fish made a swim bout, the fish stochastically received visual feedback (i.e., backward flow) or no feedback. The dynamics and peak velocity of the feedback flow were fixed, regardless of the properties of the swim bout (STAR Methods). In addition, backward flow with the same dynamics as the fixed feedback was sometimes presented in open loop, in the absence of

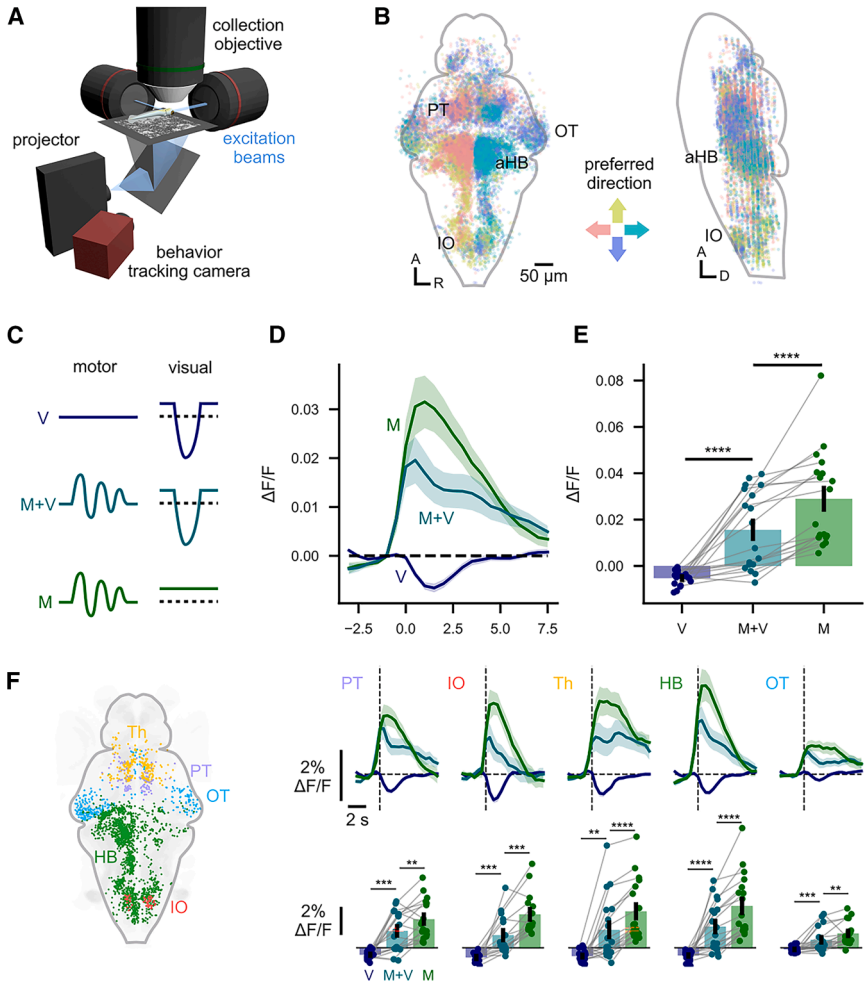

Figure 6. Neurons tuned to forward optic flow receive a positive efference copy signal

(A) Schematics of the light-sheet microscope. A pair of excitation objectives delivered perpendicular sheets of excitation beam, which moved in the Z direction in synchrony with the collection objective, allowing fast volumetric imaging.

(B) Direction-selective neurons in the (left) horizontal and (right) sagittal views. Pooled across $N = 18$ fish. See Figures S6A and S6B for traces used for identifying these cells.

(C) Schematics of the experiment. Under the presence of a constant forward optic flow, fish received the backward flow in an open loop (V), swam and received a fixed backward feedback (M + V), or swam without feedback (M).

(D) Calcium activity triggered by the three types of events, averaged across all the forward-tuned cells. The solid lines and shaded areas respectively indicate the mean across fish and its standard error.

(E) Same as (D), but averaged within the 3-s window after the triggering event. The bars indicate the averages across fish. Each dot represents a single fish, and the data from the same fish are connected by lines.

(F) Top: same as (D), but restricted to cells in specific brain regions as color-coded in the left image. Bottom: same as (E), but for each brain region. $N = 17$, 15, 18, 18, and 18 fish for PT, IO, Th, HB, and OT. $^{*}p < 0.05$, $^{**}p < 0.01$, $^{***}p < 0.001$, $^{****}p < 0.0001$ from signed-rank tests. A, anterior; R, right; D, dorsal; PT, pretectum; IO, inferior olive; Th, thalamus; HB, hindbrain; aHB, anterior hindbrain; OT, optic tectum.

See also Figure S6.

swims. We then calculated the change of fluorescence for each cell after the three types of events (i.e., swims with or without feedback and backward flow without swims) (Figure 6C).

Figure 6D shows the triggered activity of forward-selective neurons averaged across the entire brain (see also Figures S6C and S6D). Backward flow without swims resulted in a transient dip in the activity of forward-selective cells, as expected from their tuning to forward flow. Interestingly, swims without feedback resulted in positive activity on average. This observation is not trivial, given that these cells are selected purely based on their visual response properties. After the swims with feedback, the motor-driven positive activities and the sensory reafference-driven dip in activity counteracted each other, wherein the motor component overcompensated for the dip in the majority of cells (Figure S6D). Consistent patterns were observed when we restricted our analyses to specific brain regions, including those that have been implicated in OMR generation, such as the pretectum and IO (Figures 6E, S6E, and S6F). We also found backward-tuned cells whose activity is suppressed after swim bouts (Figures S6G–S6L), suggesting some degree of directional specificity in the efference copy signals. In summary, we found optic flow-tuned neurons that receive efference copy signals that would reduce responses to reafference across various brain regions. Such neurons are likely required for the forward OMR based on the history of exafferent optic flow (Figure 2), although the current data do not constrain exactly where and how such computation is implemented.

Oscillating stimuli induce additive baseline shifting in the olivary memory cells

In the final experiment, we attempted to gain insights into how multiple timescales of the optic flow memory are implemented in the brain. A previous study identified clusters of neurons in the dorsal medulla oblongata, which integrate forward and backward optic flow with long timescales and contribute to the history-dependent OMR.[14] In addition, anatomical tracings and ablation experiments suggested that these medullary neurons affect the OMR through their projections to the IO.[14] Because the IO is a structure that is clearly delineated anatomically, unlike the medulla memory cell clusters, we decided to focus on the IO as an accessible readout of the behaviorally relevant optic flow memory process in the larval zebrafish brain. In particular, we asked if the IO neurons exhibit shunting-like behavior postulated in the conditional leak model (Figure 5F). Here, we recorded activities of IO neurons expressing GCaMP6s under the control of vglut2a:Gal4[26] using a two-photon microscope (Figure 7A).

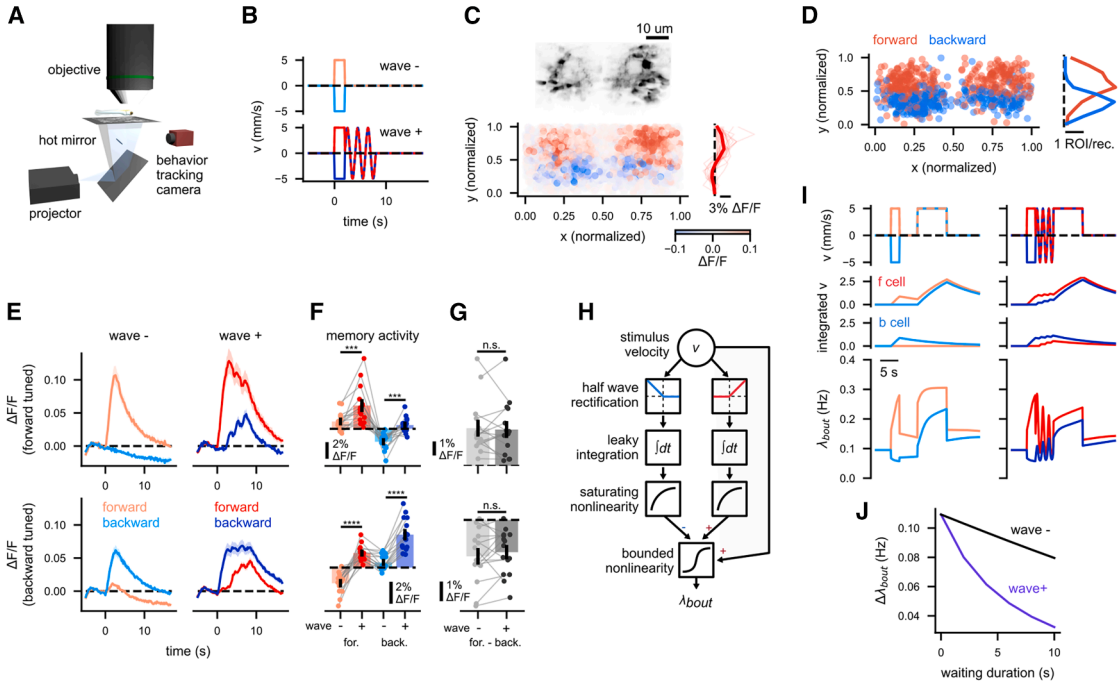

Figure 7. Increased baseline activities of the olivary memory cells in a dynamic visual environment

(A) Schematics of the two-photon microscope setup.

(B) Schematics of the visual stimuli. The fish received 2-s-long priming pulses in forward or backward directions, optionally followed by sinusoidal oscillations of the visual pattern (i.e., wave).

(C) Top: example image of the IO labeled by vglut2:Gal4. Bottom left: the IO regions of interest (ROIs) are color-coded by the difference of their response to forward- and backward-priming pulses. Pooled across 26 recordings in 15 fish. Bottom right: the median ΔF/F during the priming pulse, as a function of normalized Y (i.e., anterior-posterior) position. The bold and thin lines respectively indicate the average across 26 recordings and individual recordings.

(D) Left: the normalized positions of the ROIs that had reliable memory activity, color-coded by their preferred priming pulse directions (see STAR Methods for the detailed selection criteria). Right: the histogram of the memory cells by the normalized Y position, separately for forward- and backward-tuned cells.

(E) The response time traces of the (top) forward- and (bottom) backward-tuned memory cells to the stimuli in (B). Notice how the oscillating stimuli increase the activity of both functional cell types. The solid line and shaded areas represent the mean across fish (N = 15) and its standard error.

(F) The memory activity (i.e., the mean ΔF/F between 8 and 17 s from the priming pulse onset) by stimulus type for the (top) forward- and (bottom) backward-selective memory cells. Each dot represents an individual fish, and the data from the same fish are connected by gray lines.

(G) The difference of the memory activity by the priming pulse direction, with or without the oscillating stimuli, for the (top) forward- and (bottom) backward-selective memory cells.

(H) A schematic of the model to explain the behavior based on the IO physiology, using a saturating nonlinearity. The stimulus velocity inputs are first half-wave rectified, and the forward and backward velocities are integrated separately in a leaky fashion (τ = 15 s), which models the IO activities. The integrated velocities each undergo a saturating nonlinearity, and then they are summed together with the stimulus velocity (with appropriate sign inversions). The combined signal then undergoes a bounded nonlinearity to generate the bout frequency λ_{bout}.

(I) The simulated time traces of the (top) stimuli, (middle) integrated velocity from the forward- and backward-tuned units, and (bottom) bout frequency λ_{bout}. Note how the priming pulse directions have a lesser effect on λ_{bout} after the oscillatory stimuli.

(J) The difference in average λ_{bout} during the probe period between forward- and backward-priming conditions, as a function of the waiting duration. The model recaptures the behavior of the earlier model (Figure 5G) as well as the fish behavior (Figure 5I). n.s., not significant; $^{*}p < 0.05$, $^{**}p < 0.01$, $^{***}p < 0.001$, $^{****}p < 0.0001$ from signed-rank tests.

See also Figure S7.

In each trial, fish observed a visual pattern moving forward or backward for 2 s at 5 mm/s (i.e., priming pulse) (Figure 7B). In a subset of the trials, the priming pulse was followed by 6 s of sinusoidal, back-and-forth oscillations of the pattern (peak 5 mm/s, 0.5 Hz), as in Figure 5F. Afterward, the visual pattern stayed stationary until 17 s after the priming onset.

First, we observed that the IO cells that positively responded to the forward- and backward-priming pulses, respectively, tended to be positioned anteriorly and posteriorly, replicating the recently reported topographic pattern[27] (Figure 7C). Next, using half of the data from the trials without the oscillations, we identified "memory cells" in the IO, whose activities reliably reflected the priming pulse direction more than 6 s after its offset (see STAR Methods for the detailed selection criteria). The distribution of the forward- and backward-tuned memory cells exhibited a topographic pattern congruent to those during the priming pulse (Figure 7D). We then examined the dynamics of the responses of the memory cells using the remaining portion of the data not used for selecting those cells. Contrary to the divisive behavior of the conditional leak model (Figure 5F), the oscillatory visual motion additively increased the activity of the IO memory cells regardless of their directional preference

(Figures 7E and 7F). The increase in the forward and backward memory cell activities appeared mostly parallel (Figure 7G), and thus, the trace of the priming pulse direction is clearly discernible from the memory cell activities even after the oscillatory inputs.

Why do fish appear to become more forgetful after the oscillatory stimuli (Figure 5I), even though the IO memory cells—which are necessary for the history-dependent OMR[14]—seem to remember the optic flow happened before the oscillation? One way to reconcile these seemingly contradictory behavioral and physiological findings is to assume nonlinearity in the downstream circuitry (Figures 7H–7J and S7). For example, if we assume a saturating nonlinearity at the output of the IO memory cells, the activity differences between forward- and backward-tuned downstream cells can become smaller due to the parallel baseline shifts caused by the oscillatory stimuli, mimicking the behaviorally observed reduction in the OMR hysteresis (Figures 7H–7J). Alternatively, activity normalization between the forward- and backward-tuned populations would also result in a similar effect (Figure S7).

In summary, the observation that the IO memory cells separately integrate forward and backward cells differed from the initial shunting-based model and on its own does not explain multiple timescales of the memory-dependent OMR. However, one can still reconcile the IO physiology with the behaviorally observed shortening of the OMR hysteresis in a dynamic visual environment by speculating a simple nonlinear mechanism downstream of the IO.

DISCUSSION

The primary goal of this study was to gain a better insight into the algorithms underlying the seconds-scale history dependence in the larval zebrafish OMR. Through a series of behavioral experiments, we demonstrated that (1) the OMR depends on the recent history of exafferent, as opposed to net, optic flow, and that (2) the timescale of the OMR hysteresis is shortened in a more dynamic visual environment. Paralleling these behavioral observations, (1) we found neurons directionally tuned to the optic flow that also receive efference copy-like signals counteracting the responses to visual reafference in many brain regions, and (2) we also found that the neurons in the IO separately integrate forward and backward flow, which can explain shortening of the optic flow memory in dynamic environments by assuming a downstream nonlinearity.

As discussed in the introduction, it has remained debated what the memory-dependent component in the zebrafish OMR reflects. One possibility is that this component reflects temporally smoothed estimates of the external optic flow (flow estimation account).[9,11] Alternatively, this component might reflect path integration-based self-location memory, which would include both exafferent and reafferent optic flows (self-location memory account).[14] Our gain-manipulation experiments showed that the reafferent visual motion does not count toward the future OMR drive (Figures 2 and 3), a phenomenon more consistent with the flow estimation account. In control theoretical terms, fish appear to be performing a proportional-integral control of exafferent optic flow to nullify it, as opposed to proportional (or proportional-derivative) control over position. In light of these findings, we speculate that the medullar and olivary neurons causally connected to the history-dependent OMR[14] would be more properly characterized as holding low-pass filtered representations of velocity, rather than position, unlike other types of space-representing neurons.[19,28] Note that this is not to say that the fish never utilize reafferent optic flows: as we observed ourselves (Figure S1B), visual reafference is used to control the vigor of ongoing swim bouts in a sub-second timescale[12,15] as well as to modify the sensorimotor gain of the OMR over a longer timescale.[12,16]

How is the cancellation of the expected reafferent optic flow implemented? In the whole-brain imaging experiment, we observed efference copy-like signals in optic flow-tuned cells across diverse brain regions (Figure 6). A parsimonious hypothesis is that the subtraction of the expected reafference happens in relatively peripheral optic flow detectors (e.g., in the pretectum), which then propagate the computed exafferent signal to the other regions. Such an arrangement has been found in the optomotor circuitry in *Drosophila*[29] and the avian pretectum.[30] Alternatively, multiple optic flow-sensitive brain regions in the brain might receive efference copy signals in parallel, according to their individual functional needs. Another open question is the source of the efference copy signals. A prime candidate is the cerebellum, which has been considered to implement internal models to predict sensory outcomes of the motor commands (i.e., forward models).[31] In fact, in the specific context of the larval zebrafish OMR, we have previously shown that the cerebellar Purkinje cells are required for the fish to learn a new association between their swim bouts and the resultant visual feedback.[12] In addition, a recent study suggested that the inputs from the torus longitudinalis cancel self-generated visual inputs in the optic tectum,[32] which might explain the negative bout-triggered activities in the tectal neurons (Figures S6G–S6L).

Another major behavioral finding of this study is that the timescale of the optic flow memory depends on the stimulus dynamics (Figures 4 and 5). Although the behavioral results did not strongly constrain which specific stimulus parameters led to the shortening of the memory timescale, the models, informed with the IO physiology (Figures 7H and S7A), suggest that the sequential occurrences of flows in opposite directions are the key driver of this phenomenon. Viewed through the lens of the flow estimation account, it makes intuitive sense to be more forgetful in a rapidly changing environment, as past sensory evidence would become more quickly irrelevant to the current state that the animal is trying to estimate. Indeed, studies on normative models of decision-making have shown that ideal observers discard older evidence in a manner dependent on the environmental volatility.[33] Similarly, temporal filtering in the retinal ganglion cells becomes faster in the face of stimuli with higher variance.[34]

To better understand how the multiple timescales of the optic flow memory come about, we focused on the physiology of IO neurons. IO is a highly conserved nucleus that sends axons called climbing fibers to the cerebellum, which are typically thought to provide teaching signals that modify granule-to-Purkinje cell synapses, as well as rhythmic timing inputs to the Purkinje cells.[35] In the larval zebrafish, the IO neurons are highly sensory[27,36,37] and exhibit strongly direction-selective responses to visual[27] as well as vestibular stimuli.[37] Aside from that the IO

ablation leads to the loss of OMR hysteresis,[14] how the larval zebrafish IO activity contributes to the ongoing motor-related outputs of Purkinje cells[38] as well as cerebellar-dependent plasticity in the OMR[12] remains debated. In our recordings from the IO neurons, we observed that visual patterns oscillating back and forth increase the activity of both forward- and backward-tuned memory cells. The increase in the average activity in the face of stimuli with higher variance naturally results from the nonlinearity of neurons (as modeled in Figure S7C) and has been widely observed in early visual neurons in both vertebrates[34] and insects.[39] Yet this is somewhat surprising in the context of the optic flow detection. Optic flow-tuned neurons across taxa (e.g., primate MST,[40] mammalian[41] and avian[42] pretectum, and lobula plate tangential cells in flies[43]) are typically inhibited by the optic flow opposite to what they prefer (i.e., motion opponency), thereby representing self-motion in a signed, approximately linear fashion. The algorithmic models of the zebrafish history-dependent OMR, including our initial model (Figure 5), also implicitly or explicitly assume motion opponency before the integration step.[11,12,14] Our tentative functional interpretation of this unexpected lack of motion opponency in the IO memory cells is that, by keeping track of forward and backward motion separately, they allow the downstream circuitry to easily construct an estimate of the environmental volatility (as in Figure S7E). It is of future interest to examine how the cerebellar circuitry transforms these nonlinear memory signals in the IO.

RESOURCE AVAILABILITY

Lead contact

Requests for further information and resources should be directed to and will be fulfilled by the lead contact, Ruben Portugues (ruben.portugues@cornell.edu).

Materials availability

This study did not generate new, unique reagents.

Data and code availability

- Data generated in this study are publicly available online (Zenodo: https://doi.org/10.5281/zenodo.16085585).
- The code to analyze the data is available on the lab GitHub repository (https://github.com/portugueslab/Tanaka_2025_hysteresis).
- Any additional information required to reanalyze the data reported in this paper is available from the lead contact upon request.

ACKNOWLEDGMENTS

R.T. was supported by the European Molecular Biology Organization (EMBO ALTF 732-2022) as well as the Human Frontier Science Program (HFSP LT0027/2023-L). This research was funded by the German Research Foundation (DFG) under Germany's Excellence Strategy within the framework of the Munich Cluster for Systems Neurology (EXC 2145 SyNergy, identifier 390857198), through the "Enhanced resolution microscopy" project DFG – Projektnummer 518284373, by the Volkswagen Stiftung via a Life? grant, and by the Max Planck Gesellschaft.

AUTHOR CONTRIBUTIONS

R.T. and R.P. conceived the project. R.T. conducted the experiments, analyzed the data, and conducted the simulations. R.T. and R.P. wrote the manuscript.

DECLARATION OF INTERESTS

The authors declare no competing interests.

STAR★METHODS

Detailed methods are provided in the online version of this paper and include the following:

- KEY RESOURCES TABLE
- EXPERIMENTAL MODEL AND STUDY PARTICIPANT DETAILS
  - Zebrafish Husbandry
- METHOD DETAILS
  - Behavioral Experiments
  - Behavioral Data Analysis
  - Computational Modeling
  - Light-sheet Microscopy
  - Two-photon Microscopy
  - Stimulus Protocols for Imaging Experiments
  - Imaging data analysis
- QUANTIFICATION AND STATISTICAL ANALYSIS

SUPPLEMENTAL INFORMATION

Supplemental information can be found online at https://doi.org/10.1016/j.cub.2025.08.047.

Received: April 4, 2025
Revised: July 2, 2025
Accepted: August 20, 2025
Published: September 16, 2025

REFERENCES

1. Goldman-Rakic, P.S. (1995). Cellular basis of working memory. Neuron *14*, 477–485. https://doi.org/10.1016/0896-6273(95)90304-6.
2. Khona, M., and Fiete, I.R. (2022). Attractor and integrator networks in the brain. Nat. Rev. Neurosci. *23*, 744–766. https://doi.org/10.1038/s41583-022-00642-0.
3. Seung, H.S. (1996). How the brain keeps the eyes still. Proc. Natl. Acad. Sci. USA *93*, 13339–13344. https://doi.org/10.1073/pnas.93.23.13339.
4. Gibson, J.J. (1969). The senses considered as perceptual systems. J. Aesthet. Educ. *3*, 142–143. https://doi.org/10.2307/3331482.
5. Götz, K.G., and Wenking, H. (1973). Visual control of locomotion in the walking fruitfly Drosophila. J. Comp. Physiol. *85*, 235–266. https://doi.org/10.1007/BF00694232.
6. Messenger, J.B. (1970). Optomotor responses and nystagmus in intact, blinded and statocystless cuttlefish (Sepia officinalis L.). J. Exp. Biol. *53*, 789–796. https://doi.org/10.1242/jeb.53.3.789.
7. Orger, M.B., Smear, M.C., Anstis, S.M., and Baier, H. (2000). Perception of Fourier and non-Fourier motion by larval zebrafish. Nat. Neurosci. *3*, 1128–1133. https://doi.org/10.1038/80649.
8. Warren, W.H., Kay, B.A., Zosh, W.D., Duchon, A.P., and Sahuc, S. (2001). Optic flow is used to control human walking. Nat. Neurosci. *4*, 213–216. https://doi.org/10.1038/84054.
9. Bahl, A., and Engert, F. (2020). Neural circuits for evidence accumulation and decision making in larval zebrafish. Nat. Neurosci. *23*, 94–102. https://doi.org/10.1038/s41593-019-0534-9.
10. Barabási, D.L., Schuhknecht, G.F.P., and Engert, F. (2024). Functional neuronal circuits emerge in the absence of developmental activity. Nat. Commun. *15*, 364. https://doi.org/10.1038/s41467-023-44681-2.
11. Dragomir, E.I., Štih, V., and Portugues, R. (2020). Evidence accumulation during a sensorimotor decision task revealed by whole-brain imaging. Nat. Neurosci. *23*, 85–93. https://doi.org/10.1038/s41593-019-0535-8.

12. Markov, D.A., Petrucco, L., Kist, A.M., and Portugues, R. (2021). A cerebellar internal model calibrates a feedback controller involved in sensorimotor control. Nat. Commun. *12*, 6694. https://doi.org/10.1038/s41467-021-26988-0.

13. Portugues, R., Haesemeyer, M., Blum, M.L., and Engert, F. (2015). Whole-field visual motion drives swimming in larval zebrafish via a stochastic process. J. Exp. Biol. *218*, 1433–1443. https://doi.org/10.1242/jeb.118299.

14. Yang, E., Zwart, M.F., James, B., Rubinov, M., Wei, Z., Narayan, S., Vladimirov, N., Mensh, B.D., Fitzgerald, J.E., and Ahrens, M.B. (2022). A brainstem integrator for self-location memory and positional homeostasis in zebrafish. Cell *185*, 5011–5027.e20. https://doi.org/10.1016/j.cell.2022.11.022.

15. Portugues, R., and Engert, F. (2011). Adaptive locomotor behavior in larval zebrafish. Front. Syst. Neurosci. *5*, 72. https://doi.org/10.3389/fnsys.2011.00072.

16. Kawashima, T., Zwart, M.F., Yang, C.-T., Mensh, B.D., and Ahrens, M.B. (2016). The serotonergic system tracks the outcomes of actions to mediate short-term motor learning. Cell *167*, 933–946.e20. https://doi.org/10.1016/j.cell.2016.09.055.

17. Harden Jones, F.R. (1963). The reaction of fish to moving backgrounds. J. Exp. Biol. *40*, 437–446. https://doi.org/10.1242/jeb.40.3.437.

18. Koyama, Y., and Ueda, K. (1984). The optokinetic response of the rainbow trout Salmo gairdnerii. Bull. Jpn. Soc. Sci. Fish. *50*, 943–950. https://doi.org/10.2331/suisan.50.943.

19. Petrucco, L., Lavian, H., Wu, Y.K., Svara, F., Štih, V., and Portugues, R. (2023). Neural dynamics and architecture of the heading direction circuit in zebrafish. Nat. Neurosci. *26*, 765–773. https://doi.org/10.1038/s41593-023-01308-5.

20. Kist, A.M., and Portugues, R. (2019). Optomotor swimming in larval zebrafish is driven by global whole-field visual motion and local light-dark transitions. Cell Rep. *29*, 659–670.e3. https://doi.org/10.1016/j.celrep.2019.09.024.

21. Nykamp, D.Q., and Ringach, D.L. (2002). Full identification of a linear-nonlinear system via cross-correlation analysis. J. Vis. *2*, 1–11. https://doi.org/10.1167/2.1.1.

22. Wlodarczyk, A.I., Xu, C., Song, I., Doronin, M., Wu, Y.-W., Walker, M.C., and Semyanov, A. (2013). Tonic GABAA conductance decreases membrane time constant and increases EPSP-spike precision in hippocampal pyramidal neurons. Front. Neural Circuits *7*, 205. https://doi.org/10.3389/fncir.2013.00205.

23. Chen, X., Mu, Y., Hu, Y., Kuan, A.T., Nikitchenko, M., Randlett, O., Chen, A.B., Gavornik, J.P., Sompolinsky, H., Engert, F., et al. (2018). Brain-wide organization of neuronal activity and convergent sensorimotor transformations in larval zebrafish. Neuron *100*, 876–890.e5. https://doi.org/10.1016/j.neuron.2018.09.042.

24. Naumann, E.A., Fitzgerald, J.E., Dunn, T.W., Rihel, J., Sompolinsky, H., and Engert, F. (2016). From whole-brain data to functional circuit models: the zebrafish optomotor response. Cell *167*, 947–960.e20. https://doi.org/10.1016/j.cell.2016.10.019.

25. Portugues, R., Feierstein, C.E., Engert, F., and Orger, M.B. (2014). Whole-brain activity maps reveal stereotyped, distributed networks for visuomotor behavior. Neuron *81*, 1328–1343. https://doi.org/10.1016/j.neuron.2014.01.019.

26. Satou, C., Kimura, Y., Hirata, H., Suster, M.L., Kawakami, K., and Higashijima, S. (2013). Transgenic tools to characterize neuronal properties of discrete populations of zebrafish neurons. Development *140*, 3927–3931. https://doi.org/10.1242/dev.099531.

27. Félix, R., Markov, D.A., Renninger, S.L., Tomás, A.R., Laborde, A., Carey, M.R., Orger, M.B., and Portugues, R. (2024). Structural and functional organization of visual responses in the inferior olive of larval zebrafish. J. Neurosci. *44*, e2352212023. https://doi.org/10.1523/JNEUROSCI.2352-21.2023.

28. Yang, C., Mammen, L., Kim, B., Li, M., Robson, D.N., and Li, J.M. (2024). A population code for spatial representation in the zebrafish telencephalon. Nature *634*, 397–406. https://doi.org/10.1038/s41586-024-07867-2.

29. Kim, A.J., Fitzgerald, J.K., and Maimon, G. (2015). Cellular evidence for efference copy in Drosophila visuomotor processing. Nat. Neurosci. *18*, 1247–1255. https://doi.org/10.1038/nn.4083.

30. Yang, Y., Cao, P., Yang, Y., and Wang, S.R. (2008). Corollary discharge circuits for saccadic modulation of the pigeon visual system. Nat. Neurosci. *11*, 595–602. https://doi.org/10.1038/nn.2107.

31. Wolpert, D.M., Miall, R.C., and Kawato, M. (1998). Internal models in the cerebellum. Trends Cogn. Sci. *2*, 338–347. https://doi.org/10.1016/S1364-6613(98)01221-2.

32. Ali, M.A., Lischka, K., Preuss, S.J., Trivedi, C.A., and Bollmann, J.H. (2023). A synaptic corollary discharge signal suppresses midbrain visual processing during saccade-like locomotion. Nat. Commun. *14*, 7592. https://doi.org/10.1038/s41467-023-43255-6.

33. Kilpatrick, Z.P., Holmes, W.R., Eissa, T.L., and Josić, K. (2019). Optimal models of decision-making in dynamic environments. Curr. Opin. Neurobiol. *58*, 54–60. https://doi.org/10.1016/j.conb.2019.06.006.

34. Baccus, S.A., and Meister, M. (2002). Fast and slow contrast adaptation in retinal circuitry. Neuron *36*, 909–919. https://doi.org/10.1016/S0896-6273(02)01050-4.

35. De Zeeuw, C.I., Simpson, J.I., Hoogenraad, C.C., Galjart, N., Koekkoek, S.K., and Ruigrok, T.J. (1998). Microcircuitry and function of the inferior olive. Trends Neurosci. *21*, 391–400. https://doi.org/10.1016/S0166-2236(98)01310-1.

36. Prat, O., Petrucco, L., Štih, V., and Portugues, R. (2024). Comparing the representation of a simple visual stimulus across the cerebellar network. eNeuro *11*, ENEURO.0023-24.2024. https://doi.org/10.1523/ENEURO.0023-24.2024.

37. Migault, G., van der Plas, T.L., Trentesaux, H., Panier, T., Candelier, R., Proville, R., Englitz, B., Debrégeas, G., and Bormuth, V. (2018). Whole-brain calcium imaging during physiological vestibular stimulation in larval zebrafish. Curr. Biol. *28*, 3723–3735.e6. https://doi.org/10.1016/j.cub.2018.10.017.

38. Knogler, L.D., Kist, A.M., and Portugues, R. (2019). Motor context dominates output from purkinje cell functional regions during reflexive visuomotor behaviours. eLife *8*, e42138. https://doi.org/10.7554/eLife.42138.

39. Matulis, C.A., Chen, J., Gonzalez-Suarez, A.D., Behnia, R., and Clark, D.A. (2020). Heterogeneous temporal contrast adaptation in Drosophila direction-selective circuits. Curr. Biol. *30*, 222–236.e6. https://doi.org/10.1016/j.cub.2019.11.077.

40. Duffy, C.J., and Wurtz, R.H. (1991). Sensitivity of MST neurons to optic flow stimuli. I. A continuum of response selectivity to large-field stimuli. J. Neurophysiol. *65*, 1329–1345. https://doi.org/10.1152/jn.1991.65.6.1329.

41. Collewijn, H. (1975). Direction-selective units in the rabbit's nucleus of the optic tract. Brain Res. *100*, 489–508. https://doi.org/10.1016/0006-8993(75)90154-7.

42. Winterson, B.J., and Brauth, S.E. (1985). Direction-selective single units in the nucleus lentiformis mesencephali of the pigeon (Columba livia). Exp. Brain Res. *60*, 215–226. https://doi.org/10.1007/BF00235916.

43. Hausen, K. (1976). Functional characterization and anatomical identification of motion sensitive neurons in the lobula plate of the blowfly Calliphora erythrocephala. Z. Naturforsch. C *31*, 629–634. https://doi.org/10.1515/znc-1976-9-1001.

44. Vladimirov, N., Mu, Y., Kawashima, T., Bennett, D.V., Yang, C.-T., Looger, L.L., Keller, P.J., Freeman, J., and Ahrens, M.B. (2014). Light-sheet functional imaging in fictively behaving zebrafish. Nat. Methods *11*, 883–884. https://doi.org/10.1038/nmeth.3040.

45. Thiele, T.R., Donovan, J.C., and Baier, H. (2014). Descending control of swim posture by a midbrain nucleus in zebrafish. Neuron *83*, 679–691. https://doi.org/10.1016/j.neuron.2014.04.018.

46. Štih, V., Petrucco, L., Kist, A.M., and Portugues, R. (2019). Stytra: An open-source, integrated system for stimulation, tracking and closed-loop behavioral experiments. PLoS Comput. Biol. *15*, e1006699. https://doi.org/10.1371/journal.pcbi.1006699.

47. Štih, V., Asua, D., Petrucco, L., Puppo, F., and Portugues, R. (2022). Sashimi. Version v0.2.1. Zenodo. https://doi.org/10.5281/zenodo.5932227.

48. Pachitariu, M., Stringer, C., Dipoppa, M., Schröder, S., Rossi, L.F., Dalgleish, H., Carandini, M., and Harris, K.D. (2017). Suite2p: beyond 10,000 neurons with standard two-photon microscopy. Preprint at bioRxiv. https://doi.org/10.1101/061507.

49. Tustison, N.J., Cook, P.A., Holbrook, A.J., Johnson, H.J., Muschelli, J., Devenyi, G.A., Duda, J.T., Das, S.R., Cullen, N.C., Gillen, D.L., et al. (2021). The ANTsX ecosystem for quantitative biological and medical imaging. Sci. Rep. *11*, 9068. https://doi.org/10.1038/s41598-021-87564-6.

50. Huang, K.H., Ahrens, M.B., Dunn, T.W., and Engert, F. (2013). Spinal projection neurons control turning behaviors in zebrafish. Curr. Biol. *23*, 1566–1573. https://doi.org/10.1016/j.cub.2013.06.044.

51. Kunst, M., Laurell, E., Mokayes, N., Kramer, A., Kubo, F., Fernandes, A.M., Förster, D., Dal Maschio, M., and Baier, H. (2019). A cellular-resolution atlas of the larval zebrafish brain. Neuron *103*, 21–38.e5. https://doi.org/10.1016/j.neuron.2019.04.034.

STAR★METHODS

KEY RESOURCES TABLE

REAGENT or RESOURCE	SOURCE	IDENTIFIER
Chemicals, peptides, and recombinant proteins		
Low melting point agarose	Invitrogen	Cat#16520-100
Experimental models: Organisms/strains		
Danio rerio : wild-type Tüpfel long-fin	N/A	ZFIN: ZDB-GENO-990623-2
Danio rerio : Tg(elavl2:H2B-GCaMP6s)jf5	Vladimirov et al.[44]	ZFIN: ZDB-ALT-141023-2
Danio rerio : Tg(vglut2a:Gal4)nns20	Satou et al.[26]	ZFIN: ZDB-ALT-131127-1
Danio rerio : Tg(UAS:GCaMP6s)mpn101	Thiele et al.[45]	ZFIN: ZDB-ALT-140811-3
Software and Algorithms		
Python 3.10	N/A	https://www.python.org/
Stytra	Štih et al.[46]	https://portugueslab.com/stytra/
Sashimi	Štih et al.[47]	https://github.com/portugueslab/sashimi
suite2p	Pachitariu et al.[48]	https://www.suite2p.org/
ANTsPy	Tustison et al.[49]	https://github.com/ANTsX/ANTsPy

EXPERIMENTAL MODEL AND STUDY PARTICIPANT DETAILS

Zebrafish Husbandry

All experimental procedures were conducted according to protocols by the Technische Universität München (TUM) and the Regierung von Oberbayern (animal protocol number 55-2-1-54-2532-10112 and 55.2-2532.Vet_02-24-5). Adult zebrafish (*Danio rerio*) were housed in the fish facility in the Institute for Neuronal Cell Biology at TUM. The adult fish were maintained in water temperature of 27.5 - 28.0 °C on the 14:10 hour light:dark cycle. All experiments were performed on 6 to 8 days post fertilization (d. p. f.) larvae of undetermined sex. The Tüpfel Long-fin (TL) strain was used for all behavioral experiments (Figures 1, 2, 3, 4, 5, and S1–S5). For the whole-brain imaging experiment (Figures 6 and S6), Tg(elavl3:H2B-GCaMP6s)jf5 was used.[44] For the IO imaging experiment (Figure 7), fish carrying Tg(vglut2a:Gal4)nns20[26] and Tg(UAS:GCaMP6s)mpn101[45] were used. Fish with mutant background (mitfa$^{-/-}$) lacking melanophores were used for imaging experiments to allow optical access to the brain.

METHOD DETAILS

Behavioral Experiments

For head-fixed behavioral experiments, larvae were embedded in 1.5% low melting point agarose (Thermo Fisher) in 35 mm Petri dishes. Fish were immersed in water from the fish facility, and agarose around the tail was carefully removed so that the larvae can beat their tails. Experiments were performed at least one hour after the embedding procedure to allow fish to acclimate to the head-restrained condition. The movements of the tail were monitored with high-speed cameras at above 200 Hz under infrared illumination. Visual stimuli were projected below the fish with compact LCD projectors at approximately 60 Hz. The viewing distance was about 5 mm. Real-time tracking of the tail movements and visual stimulus generation was performed with the stytra package.[46]

To infer the intended swimming patterns of head-restrained fish, movements of the tail were analyzed as follows[46]: In each video frame, the tail of a larva was first segmented into 7 to 10 linear segments. Next, the sum of angular differences between all neighboring segment pairs were calculated, which added up to the angle between the body and the tip of the tail. We then calculated the instantaneous swim vigor of the fish as the standard deviation of this tail angle within a 50 ms rolling window. A swim bout is defined as an episode of vigor above 0.05 rad. As a proxy of turning angle at each bout, we calculated the bout bias as the cumulative sum of the tail angle within the first 70 ms in the bout, subtracted with the baseline tail angle 50 ms before the bout onset.[50]

To simulate translational and rotational optic flow, self-repeating spatial pink-noise patterns[19] were rigidly translated or rotated about the fish. Exact protocol structures are compiled in Table S1. In the closed-loop experiments, the translational and angular velocities of the stimuli were manipulated as follows: In forward OMR experiments (Figures 1, 2, 4, 5, S1, and S5), forward swimming speed of the fish was estimated by multiplying the basal gain of 30 mm/s/rad on the vigor. In the closed-loop epochs, this swim velocity was subtracted from forward stimulus velocity during swim bouts. Additional gains of 0.5 or 1.5 were applied on the forward velocity in some experiments (Figures 2, 3, S1, and S2). In the closed-loop epochs of the rotational OMR experiments, at each bout, the visual patterns were rotated by the amount specified by the bout bias multiplied by the closed-loop gain, on top of the exafferent

stimulus rotation. Reafferent rotational velocity at each bout followed the shape of a decaying exponential with a time constant of 50 ms. In each experiment, fish received either forward translational or rotational feedback only, but never both.

Behavioral Data Analysis

Behaviors of the fish were quantified in terms of the forward swim speed (or equivalently, swim vigor) or bout bias estimated online and downsampled to 20 Hz, with or without considering the closed-loop gain, depending on the context. Turning angular velocities were smoothed within 1 s rolling window when being plotted against time. These measurements were averaged across trials with the same stimulus conditions, averaged over time, correlated with or regressed by stimulus parameters, as detailed in the corresponding figure captions.

In the noise correlation experiments (Figures 4 and S4), forward or angular velocity of the stimulus $v(t)$ was determined as $v(t) = v_{base} * s(t)$ where $v_{base} = 15\,\mathrm{mm/s}$ for the forward OMR experiment and $v_{base} = 60\,^\circ/\mathrm{s}$ in the rotational OMR experiment, and $s(t) = -1$ or $+1$. $s(t)$ flipped its sign following a 0.5 Hz point Poisson process. The bout-triggered average (BTA) was calculated as $\mathrm{BTA}(\tau) = \frac{1}{N}\sum_i^N k_i v(t_i - \tau)$, where N is the number of bouts, k_i is either peak swim speed (for forward OMR) or bias (for rotational OMR) of the ith bout, and t_i is the onset timing of the ith bout. For the forward OMR experiment, bouts with the bias higher than 1 rad were excluded from the analysis. For the both experiments, fish whose bout frequency was below 0.05 Hz was excluded, as the small number of bouts made it difficult to estimate the BTA. To quantify the timescales of the computed BTA stimuli, either decaying exponential $\hat{y}(t) = y_0 e^{t/\tau}$ (for forward OMR) or logistic function $\hat{y}(t) = y_0/\left(1 + e^{\frac{t-t_0}{\tau}}\right)$ (for rotational OMR) were fit to the BTA curve from individual fish, as well as fish-averaged BTA curve. The logistic fit to the rotational BTA was chosen *ad hoc* as the sigmoid shape of the curve led to poor exponential fitting.

Computational Modeling

The conditional leak model (Figure 5) was designed to reconcile the different timescales observed in the reverse correlation and priming-delay experiments (Figure 4). The model integrator unit activity $r(t)$ followed the first-order dynamical equation $\dot{r}(t) = -(k_1 + k_2\alpha)\, r(t) + v(t)$, where $v(t)$ is the velocity of the optic flow (i. e., model input), k_1, k_2 are constants, and $\alpha = 0$ if $|v(t)| > v_{thresh}$ otherwise $\alpha = 1$. The time constant of the system becomes $\tau_1 = 1/k_1$ if $\alpha = 0$ (i. e., in the presence of optic flow) and $\tau_2 = 1/(k_1 + k_2)$ if $\alpha = 1$ (i. e., in the absence of optic flow). In Figure 5, we set k_1, k_2 such that $\tau_1 = 2.7\,s$ and $\tau_2 = 15\,s$, as well as $v_{thresh} = 1.0\,mm/s$. The model unit activity $r(t)$ was converted to the bout rate $\lambda_{bout}(t)$ by a logistic function: $\lambda_{bout}(t) = \lambda_{base} + (\lambda_{max} - \lambda_{base})/(1 + e^{-a(r(t)-b)})$, where $\lambda_{base} = 0.05\,Hz, \lambda_{max} = 2.0\,Hz$, $a = 0.27, b = 15$. For the reverse correlation simulation, bouts were stochastically simulated as a point Poisson process with a time varying bout rate $\lambda_{bout}(t)$. The reverse correlation simulation was repeated 50 times. The simulation was performed at 10 Hz.

The saturation model (Figure 7H) and the normalization model (Figure S7A) were designed to explain the multiple timescales of the OMR hysteresis (Figures 4 and 5) based on the responses of IO neurons (Figure 7). Here, the stimulus velocity $v(t)$ is first half-wave rectified: $v_+(t) = \begin{cases} v(t) \text{ if } v > 0 \\ 0 \text{ otherwise} \end{cases}$ and $v_-(t) = \begin{cases} -v(t) \text{ if } v < 0 \\ 0 \text{ otherwise} \end{cases}$. Next, the rectified velocities are separately integrated following the dynamical equation $\tau \dot{r_s}(t) = -r_s(t) + v_s(t)$, where $\tau = 15$ s and $s \in \{+, -\}$. In the saturation model, the OMR drive was computed as $d(t) = v(t) + w(f[r_+(t)] - f[r_-(t)])$ where $f[x] = 1/(1 + e^{-\beta x})$, $w = 5, \beta = 6$. In the normalization model, the OMR drive was calculated as $d(t) = v(t) + w * (r_+ - r_-)/(r_+ + r_- + \epsilon)$, where $w = 5, \epsilon = 0.01$. The bout rate $\lambda_{bout}(t)$ was then calculated in both models as $\lambda_{bout}(t) = \lambda_{base} + (\lambda_{max} - \lambda_{base})/(1 + e^{-a(d(t)-b)})$, where $\lambda_{base} = 0.05\,Hz, \lambda_{max} = 1.0\,Hz, a = 0.2, b = 15$. The simulation was performed at 10 Hz.

Light-sheet Microscopy

The custom-build light-sheet microscope used for the imaging experiments (Figures 6 and S6) was previously described in detail.[12,19] The larvae were embedded in 2.0% agarose in a custom-built rectangular chamber, and submerged in the water from the fish facility. The chamber had glass-covered windows on the front and the side to let the excitation beams in. The agarose in front of the fish was removed such that it does not scatter the excitation beams. The agarose around the tail was also removed so that the fish can move its tail. The tail movements were monitored in the same way as in the behavioral experiments. The visual stimuli were also provided in the same way as in the behavioral experiments, except that the projector outputs were filtered with a long-pass filter (Kodak Wratten No.25) to allow imaging of green fluorescence. Each fish waited at least 1 hour after the embedding procedure before entering the experiments.

The excitation was provided by a 488 nm laser source (Cobolt), which was split between two orthogonal excitation arms. The two orthogonal beams allowed us to excite cells between the eyes and posterior to the eyes without exposing the eyes. Each arm consisted of a pair of galvanometric mirrors (Thorlabs) to scan the beam vertically and horizontally, a 2x beam expander, and a low numerical aperture air objective (Olympus) that focused the beams on the brain. The fast horizontal scanning of the laser created sheets of light. The emitted fluorescence was filtered with a 525:50 band pass filter and collected with a CMOS camera (Hamamatsu), through a 20x water immersion objective (Olympus). The collection objective was equipped with a piezo drive and moved in

synchrony with the sawtooth-patterned vertical scanning of the light sheets, achieving the volumetric imaging. The resultant spatio-temporal resolution of the data was around 15 x 0.6 x 0.6 microns per voxel at 2 Hz. The control of the microscope was provided by a custom written software.[47]

Two-photon Microscopy

For the two-photon microscopy experiments (Figure 7), animals were embedded in a 35 mm petri dish in 2.0% agarose, in the same way as in the behavioral experiments. The visual stimuli were presented from below, and long-pass filtered in the same way as in the light-sheet imaging experiment. The excitation was provided by a femtosecond pulsed laser at the wavelength of 920 nm (Spark ALCOR 920-2) through a high NA, 20x water-immersion objective (Olympus). The average power at the sample was approximately 10 mW. The emitted fluorescence was filtered with a 750 nm short pass and a series of two band pass filters (535:40, 525:39). The scanning head consisted of a horizontally scanning resonant mirror (12 kHz) and a vertically scanning galvanometric mirror, controlled by custom-written software through a National Instruments FPGA. The pixels were sampled at 20 MHz and averaged 8-fold, resulting in the 5 Hz frame rate with the image size of approximately 500 x 600 pixels and the resolution of about 0.2 micron per pixel.

Stimulus Protocols for Imaging Experiments

At the beginning of each light-sheet imaging experiment (Figure 6), the pink noise pattern moving in the four directions (forward, backward, left, right) at 15 mm/s were presented in an open loop. Each movement lasted 5 seconds with 5 seconds of interleaves, and each direction was repeated 5 times. Next, the fish observed a continuous forward movement of the pink noise pattern at 5 mm/s for 30 minutes. During this period, swim bouts of the fish triggered visual feedback with a fixed velocity profile in a stochastic manner (superimposed on the constant flow). The feedback velocity was defined as $v_{fb}(t) = v_{max}(et/t_{peak})^p e^{-t/\tau}$ where $p = t_{peak}/\tau$ and t is the time since the bout onset. Here, $v_{fb}(t_{peak}) = v_{max}$ and τ controls the fall-off. The parameters were set to mimic the vigor profile of a typical forward bout during the OMR ($v_{max} = 50\ \mathrm{mm/s}, t_{peak} = 50\ \mathrm{ms}, \tau = 100\ \mathrm{ms}$). To dissociate the effects of the motor activity and visual feedback, for 50% of the bouts, visual feedback was not provided. In addition, pulses of backward flows with the same profile as described above were stochastically presented in the absence of bouts at the mean rate of 0.5 Hz, if fish made no bouts for more than 3 seconds.

The two-photon imaging experiment on the IO neurons (Figure 7) also started with the repeated presentation of the pink noise pattern moving in four directions as in the light-sheet imaging, but this portion of the data was not analyzed. The remaining of the experiment consisted of repetitions of 22 s long trials, which were all in an open-loop. At the beginning of each trial, a self-repeating pink noise pattern was reset to a random position. After an initial wait of 5 seconds, the pattern moved forward or backward for 2 seconds ("priming pulse"). In a subset of trials, immediately following the priming pulse, the pattern oscillated back and forth at 0.5 Hz with the peak speed of 5 mm/s. For the rest of the trial, the pattern remained stationary. Trials with and without oscillations were respectively repeated for 24 and 12 times for each priming pulse direction.

Imaging data analysis

We used the suite2p package[48] to rigidly align the frames and to extract regions of interests (ROIs) from the raw calcium imaging movies, for both light-sheet and two-photon data. Briefly, suite2p iteratively aligns the movie to randomly picked reference frames using phase-correlation. To find neuronal somas, suite2p performs singular value decomposition on the movie and looks for peaks in the spatial singular vectors after smoothing. For the light-sheet imaging data, the aligned, time-averaged volumetric images of each brain were then registered to the MapZBrain atlas reference brain[51] using ANTsPy[49] in two steps: an affine transformation based on manually defined key-points, and a non-rigid, diffeomorphic registration. The coordinates of the ROIs in the MapZBrain space is calculated using this registration, and their affiliation to different brain regions were determined using anatomical masks provided on the MapZBrain. For the two-photon imaging data on the IO neurons, manual rectangular masks were drawn around the IO, according to which the ROI coordinates were normalized.

For the experiment in Figure 6, we first identified direction selective visual neurons as follows: First, within the initial section during which translational motion was presented, the fluorescence time trace of each ROI $F(t)$ was normalized into $\Delta F/F = (F(t) - F_0)/F_0$, where the baseline F_0 was defined to be the 1st percentile value of the raw fluorescence during this period. Next, the Pearson correlations of the normalized fluorescence between every pair among the five repetitions of the translational stimuli were calculated and averaged. Only ROIs with the averaged correlation above 0.4 are considered to be reliable visual neurons. Third, direction selectivity index (DSI) was calculated as $DSI_d = (r_d - r_{\bar{d}})/(r_d + r_{\bar{d}})$ where r_d is the time- and repetition-averaged normalized fluorescence during the presentation of motion in direction $d \in \{\mathrm{left}, \mathrm{right}, \mathrm{forward}, \mathrm{backward}\}$, and $\bar{d}$ is the opposite direction of d. We considered an ROI to be selective for direction d only if $DSI_d > 0.4$ as well as $r_d \geq r_D$ for all $D \in \{\mathrm{left}, \mathrm{right}, \mathrm{forward}, \mathrm{backward}\}$. If fish exhibited highly reliable behavior in response to the repeated translational stimuli, motor neurons might pass these criteria for the response reliability and direction selectivity. To make sure this is not the case, we created a binary time trace of swim bouts $b(t)$ for the initial 200 s section during which the translational stimuli were presented, where $b(t) = 1$ at the onsets of swim bouts and 0 elsewhere. We then smoothed $b(t)$ with a decaying exponential with a time constant of 2.0 s to account for the kinetics of the calcium indicator, and correlated the fluorescence of each cell with this smoothed bout traces. We observed that the direction selective cells we identified generally had correlation to the bout traces below the average pairwise correlation to repeated stimulus presentations (Figure S6B). As such, we did not perform further screening to exclude motor-like neurons from our dataset.

For each of direction selective cell we identified as above, we calculated the triggered averages of the fluorescence for each of the three events (i.e., bouts without feedback, bouts with feedback, and backward flows without bout). Here, the raw fluorescence was converted to $\Delta F/F$, using the average fluorescence during the 3 seconds preceding the onset of each event as F_0. The triggered averages were then averaged across ROIs and fish (for visualizations of response dynamics), as well as across ROIs and over time within the 3 second window after the event onset within each fish (for statistical comparisons).

The two-photon imaging data on the IO (Figure 7) was first converted into $\Delta F/F$for each ROI and each ROI, using the average fluorescence during the initial 5 second waiting period as F_0. For each ROI, $\Delta F/F$ was averaged over time within a 2-s window during the priming phase (“early activity”), as well as within the last 9 seconds of the trial (“late activity”). Next, repetitions of the trials without the oscillatory stimuli were split into two halves (i.e., training and test sets). The training set priming response difference $\Delta\mu_e = \mu_{fe} - \mu_{be}$, where μ indicates the mean forward early (fe) and backward early (be) activities, were calculated to examine the general topographic pattern of the direction selectivity in the IO (Figure 7C). To select ROIs that exhibited memory-like activity, for each ROI, Z-scored difference $Z_l = \frac{\mu_{fl} - \mu_{bl}}{\sqrt{\frac{\sigma_{fl}^2}{N} + \frac{\sigma_{bl}^2}{N}}}$ was calculated, where μ and σ^2 respectively indicate the mean and variance of the forward late (fl) and backward late (bl) activities, and N is the number of repetition (i.e., 12). ROIs with $|Z_l| > 2$ and congruently signed Z_l and $\Delta\mu_e$ were selected as “memory cells”. The activities of memory cells were averaged across trials and ROIs within each fish for each condition (only using the test set for the conditions without oscillations), and then across fish, for the dynamics visualization (Figure 7E). The late activity was averaged within each fish to make comparisons across stimulus conditions (Figures 7F and 7G).

QUANTIFICATION AND STATISTICAL ANALYSIS

For pair-wise comparisons of time-averaged behaviors or neural responses within each fish across conditions or against 0, we used Wilcoxon signed-rank tests. For comparisons across multiple levels of independent variables, Friedman’s chi square tests were used. The sample sizes (i.e., the number of animals) as well as the definition of the lines and shades (typically mean and its standard error across animals) can be found in the captions of the corresponding figures.